



Research Article

Bolivian hornblendite cumulates: Insights into the depths of Central Andean arc magmatic systems

L.C. Velázquez Santana^{a,*}, C.L. McLeod^a, D. Blakemore^a, B. Shaulis^b, T. Hill^c^a Department of Geology and Environmental Earth Science, Miami University, 250 S Patterson Avenue, Oxford, OH, 45056, USA^b Trace Element and Radiogenic Isotope Lab, University of Arkansas, Fayetteville, AR 72701, USA^c Bruker Nano, Inc., 5465 E. Cheryl Parkway, Madison, WI 53711, USA

ARTICLE INFO

Article history:

Received 26 January 2020

Received in revised form 31 May 2020

Accepted 1 June 2020

Available online 05 June 2020

Keywords:

Hornblendites

Cumulates

Central Andes

Continental arc magmatism

Amphibole fractionation

ABSTRACT

The eruptive products of continental arc volcanoes provide wide-ranging insights into the processes governing storage, differentiation, and final eruption (or emplacement) of magmas from trans-crustal magmatic systems. The important role and fractionation of amphibole in continental arc magmatic systems is well documented even if amphibole is generally absent as a prevalent phenocrystic phase in erupted, differentiated lavas. This study presents a comprehensive textural and geochemical investigation of rare plagioclase-bearing hornblendite cumulates entrained in c. 1.4 Ma (trachy-)andesites at the Quillacas monogenetic center on the Bolivian Altiplano, Central Andes. MicroXRF mapping and imaging via SEM-EDS clearly reveals their mesocumulate, idiomorphic nature characterized by cumulus hornblende ($\geq 90\%$) with intercumulus sodic plagioclase (~8%), minor Fe-Ti oxides and accessory apatites. The trace element compositions of cumulus amphiboles are consistent with their crystallization from a silicate melt with $(La/Yb)_N < 5$ and low $(Pb/Ce)_N$ at < 0.6 . Amphibole TiO_2 contents imply crystallization between 700 and 764 °C consistent with depths in the arc crust of 50–55 km as constrained by the Central Andean geotherm. Bulk hornblendite isotopic signatures (Sr-Nd-Pb) correspond to compositions associated with the Central Andean mid-lower arc crust consistent with the presence of hornblendite cumulate piles at this depth. Intercumulus (titano)magnetite exhibits oxy-exsolution ilmenite lamellae, the formation of which is associated with oxygen fugacity (fO_2) increase during magmatic cooling and differentiation. The ubiquitous presence of gabbroic dehydration (reaction) rims (20–40 μm in width) on the amphiboles is interpreted to be the result of a decrease in fO_2 during ascent. The hornblendite mesocumulates from this study validate the extensive “cryptic” fractionation of amphibole at arcs and its important role on the petrogenesis of (continental) arc magmas.

© 2020 Elsevier B.V. All rights reserved.

1. Introduction

Investigating the petrological and geochemical nature of magmatic plumbing networks is crucial to advancing our understanding of the evolution of these systems within the Earth's crust (e.g. Blundy and Cashman, 2008; Holness et al., 2019; Rivera et al., 2014). For the past several decades, study of the differentiated extrusive products of these magmatic systems has provided new insights into, and constraints on, the nature of the storage conditions within magma reservoirs at depth (e.g. Barboni et al., 2016; Jackson et al., 2018; Shane and Smith, 2013; Szymanowski et al., 2017), the production of, and interaction between, distinct crystal cargoes (e.g. Davidson et al., 2005; Ganne et al., 2018; Marsh, 2006), and the timescales associated with eruption cycles, crystal residence times, and recharge events (e.g. Cooper, 2019; Schleicher et al., 2016; Triantafyllou et al., 2020). Collectively, these efforts have

contributed to a “paradigm shift” in the communities' understanding of magmatic reservoirs where instead of magma storage occurring in large, melt-dominated systems, hot regions of crystal-rich bodies (or “liquid-poor crystal mushes”) exist throughout the lithosphere (Holness et al., 2019).

Extrusive magmatism at continental arcs records the complex interaction between subducting dehydrating oceanic lithosphere, primary arc magmas, and the overriding continental lithosphere (Gill, 1981). Continental arcs have been the intense focus of study for decades in part due to the compositional similarity between erupted, andesitic-dacitic products and bulk geochemical characteristics of Earth's continents (e.g. Kelemen et al., 2004; Shirey and Hanson, 1984; Taylor and White, 1965). Over time, continental arcs are proposed to mature and produce stable continental crust (although a petrogenetic link between modern-day arcs and crustal production remains challenging to establish; Ducea et al., 2015). In the case of the Andean arc of western South America, the type-example of continental arc magmatism on modern-day Earth, a long-history of arc magma production and

* Corresponding author.

E-mail address: velazqlc@miamioh.edu (L.C. Velázquez Santana).

differentiation exists (e.g. Beck and Zandt, 2002; Dewey and Lamb, 1992; Pepper et al., 2016). In these environments, magma mixing, magma mingling, crustal assimilation, and fractional crystallization are the primary factors influencing the mineralogy, petrology, and bulk geochemistry of magmatic activity (e.g. Edmonds et al., 2019; Farner and Lee, 2017). Compositionally, magmas erupted at continental arcs are dominated by intermediate compositions often attributed to the mixing and mingling of mafic and silicic endmembers before eruption (e.g. Reubi and Blundy, 2009) with primitive end-member compositions rarely recorded in the erupted products. This is particularly true in the case of the Central Andes where no 'true' basalts have been erupted in the past ~5 Ma and the erupted products are dominated by mineralogically and chemically evolved andesitic to rhyolitic compositions (e.g. Brandmeier and Wörner, 2016; Kay et al., 2014). Researchers have recently reconsidered the conventional "magma chamber" model to account for the recorded heterogeneity that exists within the geochemical record of magmatic arc systems. The proposed trans-crustal magmatic system (TCMS) model suggests that after the melt is extracted from the upper mantle, it traverses through the lower crust, the mid crust (where it possibly 'pools' in arcs), and then the upper crust; finally, the melt is stored/stalled in the shallow crust where crystallization and assimilation can occur before eruption (Cashman et al., 2017; Marsh, 2006). Chemical, textural, and mineralogical heterogeneity within erupted products can thus be attributed to the presence of various crustal storage zones in which stalling, cooling, crystallization, and differentiation may occur at any stage throughout the magmatic plumbing system (Cashman et al., 2017; Edmonds et al., 2019; Marsh, 2006; Smith, 2014). As multiple crustal storage zones can exist, evaluating the petrogenetic pathway of arc magmas from source to surface is necessary.

Amphibole is a near-ubiquitous fractionating phase in arc magmas, as is often recorded in erupted lava geochemistry (e.g. Davidson et al., 2007; Dessimoz et al., 2012; Garcia and Jacobson, 1979) and plays a fundamental role in the geochemical evolution of arc magmas. At intermediate crustal depths, combined with elevated H₂O contents, all the necessary components for amphibole fractionation are present (Fischer and Marty, 2005; Wallace, 2005). However, amphibole is not a ubiquitous phase in erupted arc products and can therefore be considered as a "cryptic" fractionating phase (Davidson et al., 2007; Kratzmann et al., 2010; Smith, 2014).

In this study, new mineralogical, petrological, and geochemical data for a suite of hornblende-plagioclase-apatite-bearing mafic enclaves, henceforth termed "hornblendites" are presented. Entrained in c. 1.4 Ma andesites, the sampled hornblendites were erupted at the Quillacas monogenetic volcanic center located in the back-arc region of the Bolivian Altiplano, Central Andes (Davidson and de Silva, 1992, 1995). These hornblendites record the near-ubiquitous, yet "cryptic" fractionation of amphibole in intermediate arc magmas. The aim of this study is therefore to: 1) comprehensively characterize the mineralogical, textural, chemical, and physical characteristics of the hornblendites and 2) evaluate their petrogenesis within the context of arc magma genesis at continental arcs. Collectively, this dataset aims to advance the understanding of the role of amphibole in TCMS beneath continental arcs (Plail et al., 2018; Scroggs and Putirka, 2018).

2. Field area

The Andean Cordillera (Fig. 1a) can be divided into several volcanically active zones: Northern Volcanic Zone (NVZ), Central Volcanic Zone (CVZ), Southern Volcanic Zone (SVZ), and the southerly Austral Volcanic Zone (AVZ). These zones are defined by areas where surface expression of volcanism is absent due to flat slab subduction (e.g. Bishop et al., 2017; Sørensen and Holm, 2008). The primary focus of this study is the Central Andean Cordillera (16°–22°S) where the continental basement extends to c. 80 km in depth beneath the modern-day Bolivian Altiplano due to tectonic shortening of the weaker western

region of the South American plate between stronger lithospheres: the subducting Nazca plate and the underthrusting Brazilian Shield (Beck and Zandt, 2002; Zandt et al., 1994). As shown in Fig. 1b, a suite of monogenetic volcanic centers is exposed across the Bolivian Altiplano back-arc and behind-arc regions. These volcanic centers broadly range in age from Pliocene to Holocene and from basaltic andesite to dacite in composition (basalts exist but are rare; Davidson and de Silva, 1992, 1995). Specifically, the minor center of Quillacas (QL) is one of the easternmost centers located on the Bolivian Altiplano. Here, c. 1.4 Ma andesitic lava is host to a suite of chemically diverse crustal xenoliths (Davidson and de Silva, 1995; McLeod et al., 2012, 2013) and several hornblendites that were originally classified as mafic enclaves. While the nearby center of Pampa Aullagas (PA) (Fig. 1b) also contains abundant crustal xenoliths, the hornblende enclaves are unique to QL. Occurrence of xenolithic material in continental arc volcanics is rare, most likely due to the thick and ductile nature of the underlying basement (Weber et al., 2002). Therefore, the materials entrained within the QL lavas offer an exceptional opportunity to investigate and constrain the components of TCMS in this region.

3. Sample petrography

Sampled hornblendites are dominated by medium-coarse grained hornblendes (≥90%), sodic plagioclase (~8%), with minor (titano)magnetite and accessory apatite as interstitial phases (Fig. 2) and are classified here as plagioclase-bearing hornblendites (Supplementary Fig. 1). The hornblendes are typically euhedral and granular in nature with opaque rims characterizing crystal edges. No hornblende crystals are observed to lack these rims and the majority of crystals are inclusion free. Single twins are commonly observed consistent with a magmatic origin for the hornblendes (Supplementary Fig. 2; Triantafyllou et al., 2016). Plagioclase feldspars are anhedral and interstitial in nature (Fig. 2a-d). Accessory apatites are euhedral to subhedral with bladed habits and are clearly interstitial, at times appearing to be interlocked with the edges of the hornblendes.

Backscattered electron (BSE) images acquired via scanning electron microscopy (SEM) and elemental maps acquired via energy dispersive x-ray spectroscopy (EDS) are shown in Fig. 3. Hornblendes are consistently large with average maximum lengths between 700 and 800 μm with some grains exceeding 1 mm. Hornblende cleavage (56°–124°) is clearly discernible. The rims of the grains exhibit complex textures with at least three discernable, smaller mineral phases distinguished via atomic mass contrast (Fig. 3a-d). Apatites are prismatic and demonstrate a variety of grain sizes between 50 and 75 μm in width and 100–200 μm in length (Fig. 3d). (Titano)magnetite and ilmenite are also present in minor amounts throughout the samples as interstitial phases. Fig. 3e illustrates an anhedral (titano)magnetite (200 μm) surrounded by a "halo" of smaller grains. The majority of (titano)magnetite crystals in the hornblendites exhibit rhombohedral ilmenite exsolution lamellae (Fig. 3f).

4. Results

4.1. Elemental mapping via micro x-ray fluorescence (μXRF) and scanning electron microscopy (SEM).

Elemental maps of hornblende thin sections were acquired via μXRF (Fe, Ca, and Ti) and are shown in Fig. 4a-f. The distribution of Fe, Ca, and Ti across the samples is consistent with the occurrence of hornblende, sodic plagioclase, minor Fe-Ti oxides, and accessory apatite. Figs. 4 g-r summarize Fe, Ca, Ti, and Na distributions acquired via SEM-EDS and highlight the occurrence, although rare, of Fe zonation within the amphibole populations (e.g. Fig. 4k). Accessory apatite is distributed between coarser-grained amphiboles with interstitial sodic plagioclase (e.g. Fig. 4j). The presence of minor (titano)magnetite and associated oxy-exsolution ilmenite lamellae are shown in Fig. 4o, q.

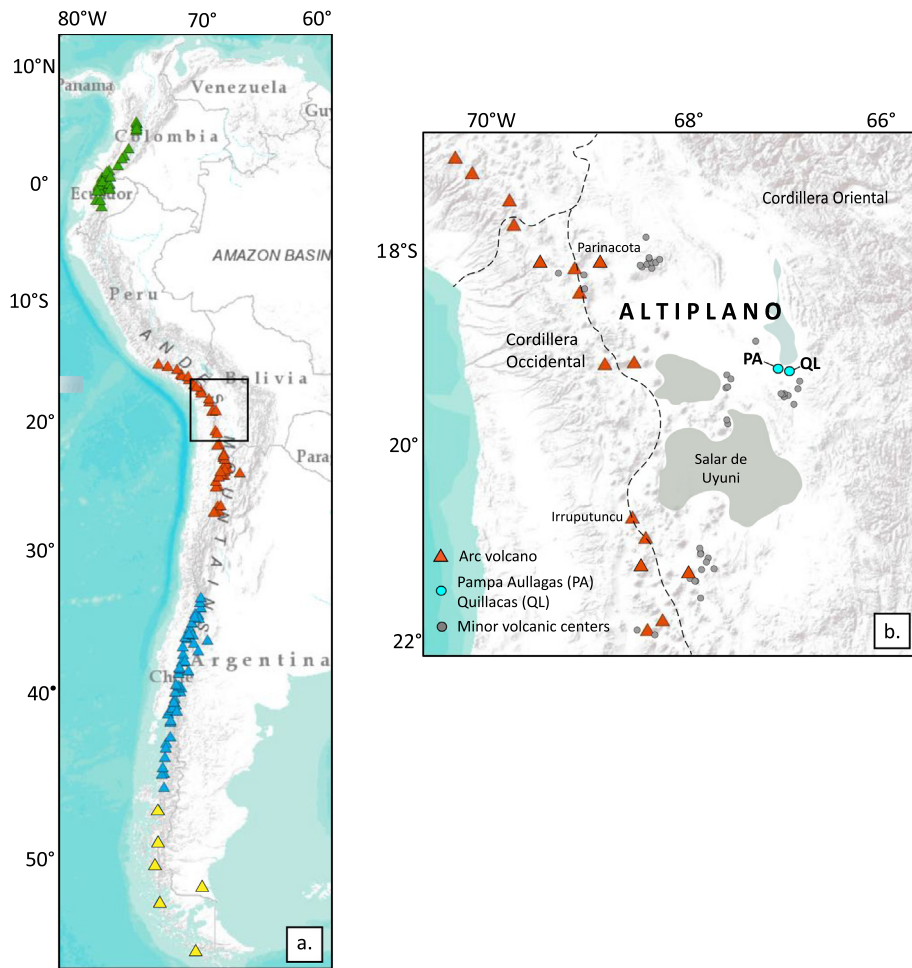


Fig. 1. **a** Terrain map of the Andean Cordillera, South America denoting four volcanic zones: Northern Volcanic Zone (NVZ; green), Central Volcanic Zone (CVZ; orange), Southern Volcanic Zone (SVZ; blue), and Austral Volcanic Zone (AVZ; yellow). **b** Map highlighting the CVZ, major arc volcanoes (orange triangles), and back-arc monogenetic volcanic centers (grey circles) located across the Bolivian Altiplano. The Pampa Aullagas (PA) and Quillacas (QL) monogenetic volcanic centers (blue circles) on the Eastern Altiplano are the focus of this study. (For interpretation of the references to colour in this figure legend, the reader is referred to the web version of this article.)

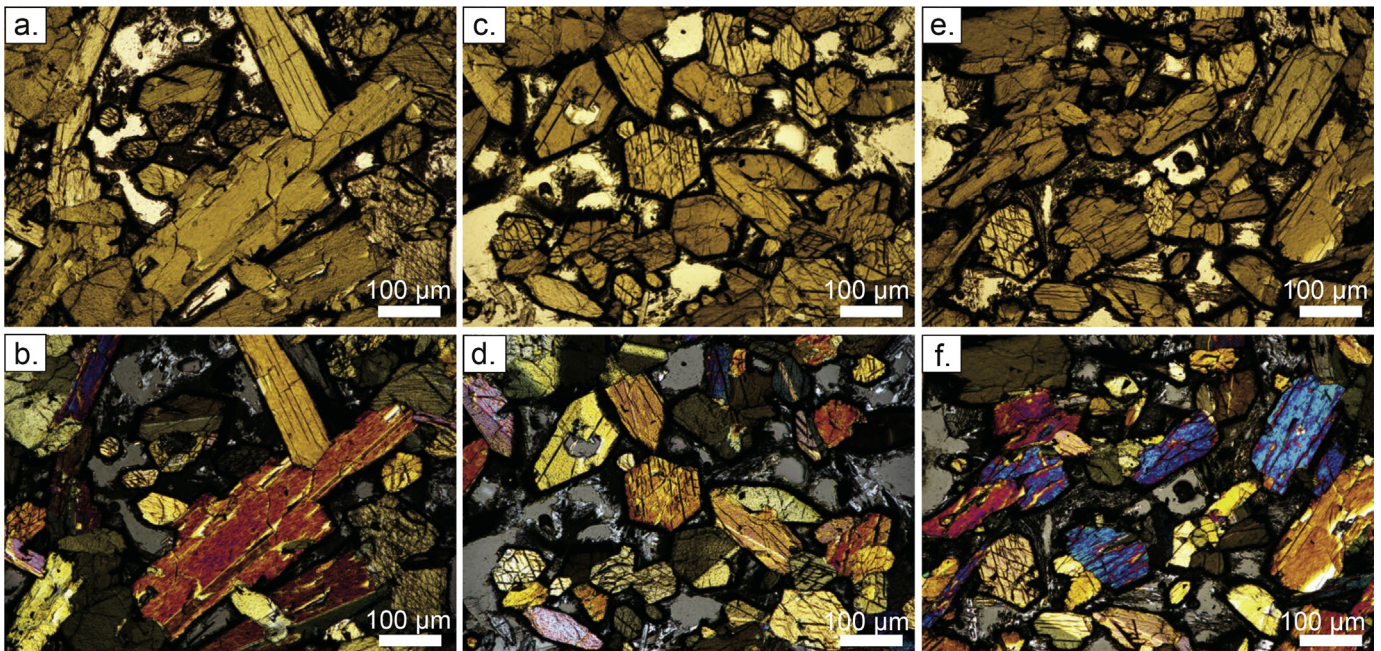


Fig. 2. **a-f** Photomicrographs denoting the representative mineral assemblage of the hornblendite suite. Plane-polarized light (PPL) images are shown in the upper row. Corresponding cross-polarized light (XPL) images are shown in the lower row.

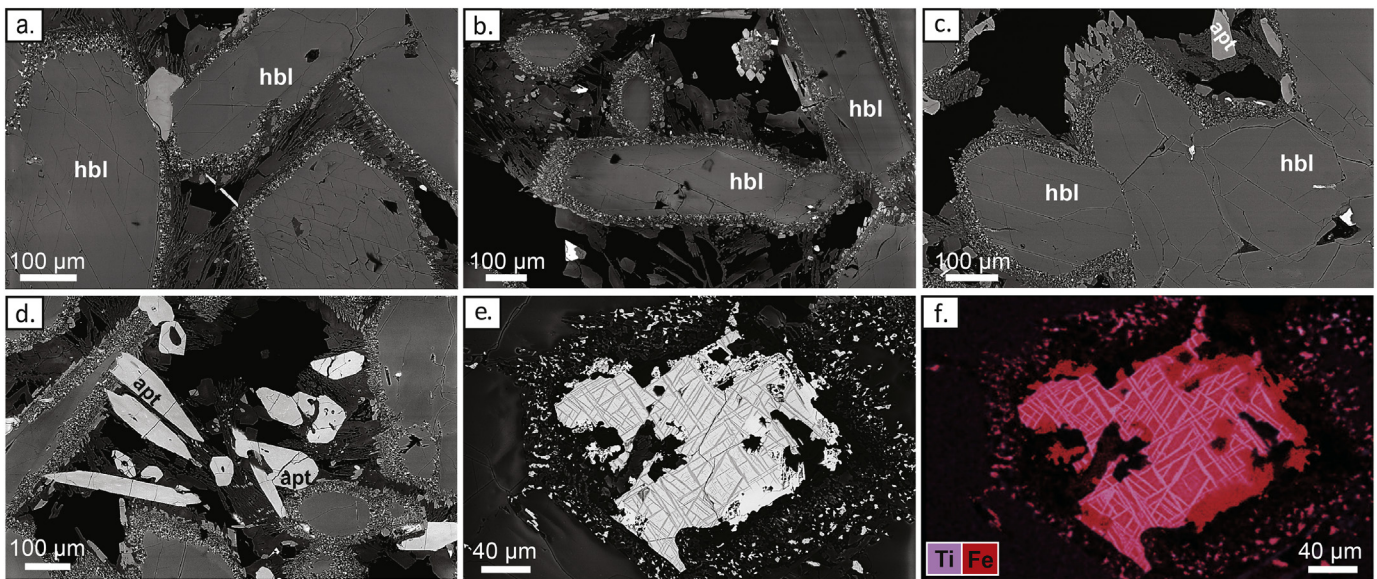


Fig. 3. Scanning electron microscopy (SEM) back-scattered electron (BSE) images and energy dispersive x-ray spectroscopy (EDS) elemental map collected on hornblende thin sections. **a–c** Euhedral hornblende crystals (700–800 μm , hbl) are the predominant phase throughout the sample suite (labelled in 3a–c). **d** Prismatic apatites (apt) are present as an accessory phase and are commonly found in close spatial association with the rims of hornblende. **e** Anhedral titanomagnetite (200 μm) surrounded by a “halo” of smaller crystals. **f** Corresponding SEM-EDS map of **e** demonstrating rhombohedral ilmenite exsolution lamellae. Further descriptions are provided in the main text.

4.2. Bulk major and trace elements

Fig. 5a–h summarizes the bulk major element oxides for the sampled hornblendites (Supplementary Table 1). Also shown is the average bulk composition of their host QL lavas and the compositional field for age-equivalent (< 2 Ma) Central Andean lavas. Data for arc-related hornblendites from New Zealand (early Cretaceous arc), Kohistan (Cretaceous arc), and Morocco (Neoproterozoic arc) are shown for comparison (Daczko et al., 2012; Dhuime et al., 2007; Triantafyllou et al., 2018). The Central Andean hornblendites exhibit small variations in their bulk major element content but, as a suite, they are compositionally homogeneous. Bulk SiO_2 content are primitive at 43.55–44.89 wt% and TiO_2 content are high from 2.47 to 2.66 wt%. Total alkalis are low ($\text{Na}_2\text{O} + \text{K}_2\text{O}$ from 3.55 to 3.74, not shown) but CaO wt% are high at 10.39 to 10.81. Compositionally, all of the hornblendites summarized in **Fig. 5** exhibit low silica, ranging from 40 to 50 wt% SiO_2 with those from the Central Andes ($n = 7$), Kohistan ($n = 1$), and New Zealand ($n = 6$) ranging from 40 to 45 wt% SiO_2 . Considering other major oxides, bulk compositions are broadly similar with the most notable differences between Moroccan hornblendites and the other localities with respect to TiO_2 and Al_2O_3 . This could be attributed to the absence of ilmenite \pm magnetite, rare rutile and titanite, and the late-stage crystallization of volumetrically minor plagioclase in those samples (Triantafyllou et al., 2018). The calculated Mg# (molar $100 \times \text{MgO}/(\text{MgO} + \text{FeO}_{\text{tot}})$) for Central Andean hornblendites range from 67 to 70 and are shown in **Fig. 5i** vs. wt% Al_2O_3 alongside other hornblendite localities. The majority of Mg# values shown overlap with the composition of primary melts that are in equilibrium with Fo_{90} mantle olivine (Roeder and Emslie, 1970) although hornblendites from Morocco and New Zealand are higher (Mg# > 74).

A primitive mantle normalized multi-element diagram for the sampled hornblendites is shown in **Fig. 6a**. For comparison, **Fig. 6a** includes the primitive-mantle normalized patterns of hornblendites from the three arcs discussed in **Fig. 5**. The range of compositions associated with age-equivalent Central Andean volcanic rocks are also shown for comparison (grey shaded region, all < 2 Ma). As shown, the Central Andean hornblendites are relatively homogenous. They exhibit moderate large ion lithophile element (LILE) enrichment (Rb_N : 26.9–30.7; Ba_N : 504–582) relative to Central Andean lavas and display flat Th_N to Ce_N

signatures (Th_N : 23.7–26.0; Ce_N : 19.4–20.0), with no Nb-Ta depletion. Zirconium (Zr) presents a negative anomaly (Zr_N : 6.02–7.18) which is expected as D_{Zr} in amphibole is typically < 1, particularly for mafic to ultramafic lithologies (D_{Zr} : 0.13–0.37; Adam et al., 1993; Sisson, 1994; LaTourrette et al., 1995). Therefore, a negative anomaly suggests higher Zr concentration in residual evolved melt after fractional crystallization. Collectively, the hornblendites exhibit enrichment peaks in Ba and Pb along with Zr-Hf depletion. Patterns from the hornblendites of this study are similar to those of the Neoproterozoic Bougmane arc hornblendites (Triantafyllou et al., 2018) but are consistently enriched in all shown trace elements compared to the other sample suites. Hornblendites from the Cretaceous Kohistan and New Zealand arcs (Daczko et al., 2012; Dhuime et al., 2007) exhibit similar normalized patterns and are depleted in some elements compared to Central Andean hornblendites by several orders of magnitude (e.g. Th, U, Nb, La). **Fig. 6b** summarizes the chondrite normalized rare-earth element (REE) signatures for Central Andean hornblendites and their host QL lavas, alongside recent Central Andean lavas and other hornblendite suites. The Central Andean hornblendites of this study are compositionally homogeneous exhibiting slight LREE depletion (La_N/Pr_N : 0.63–0.67) with decreasing normalized concentrations from Pr to Lu (Pr_N/Lu_N : 7.6–8.1). Europium (Eu) anomalies are minor with Eu/Eu^* ranging from 0.82–0.91 ($n = 4$). Consistently, the Central Andean hornblendites are more REE-enriched than other hornblendite suites and have an overall pattern similar to that of the Bougmane arc hornblendites, although the latter exhibit flatter MREE-HREE patterns (Pr_N/Lu_N : 2.4–3.8). Their Eu-anomalies are also similar ranging from 0.83 to 0.89 ($n = 6$). Hornblendites from the New Zealand and Kohistan arcs are both significantly LREE-depleted (La_N/Pr_N : 0.35–0.39; 0.25, respectively). New Zealand arc hornblendites exhibit similar MREE-enrichment and HREE-depletion to hornblendites from this study (Pr_N/Lu_N : 6.4–8.2).

4.3. Amphibole and apatite trace elements

Three thin sections of the sampled hornblendites were selected for in-situ chemical analysis via LA-ICP-MS. Amphibole trace element data are presented in Table 2 of the Supplementary Material. Typical amphibole signatures show moderate LREE depletion (La_N/Sm_N : 0.43–0.57),

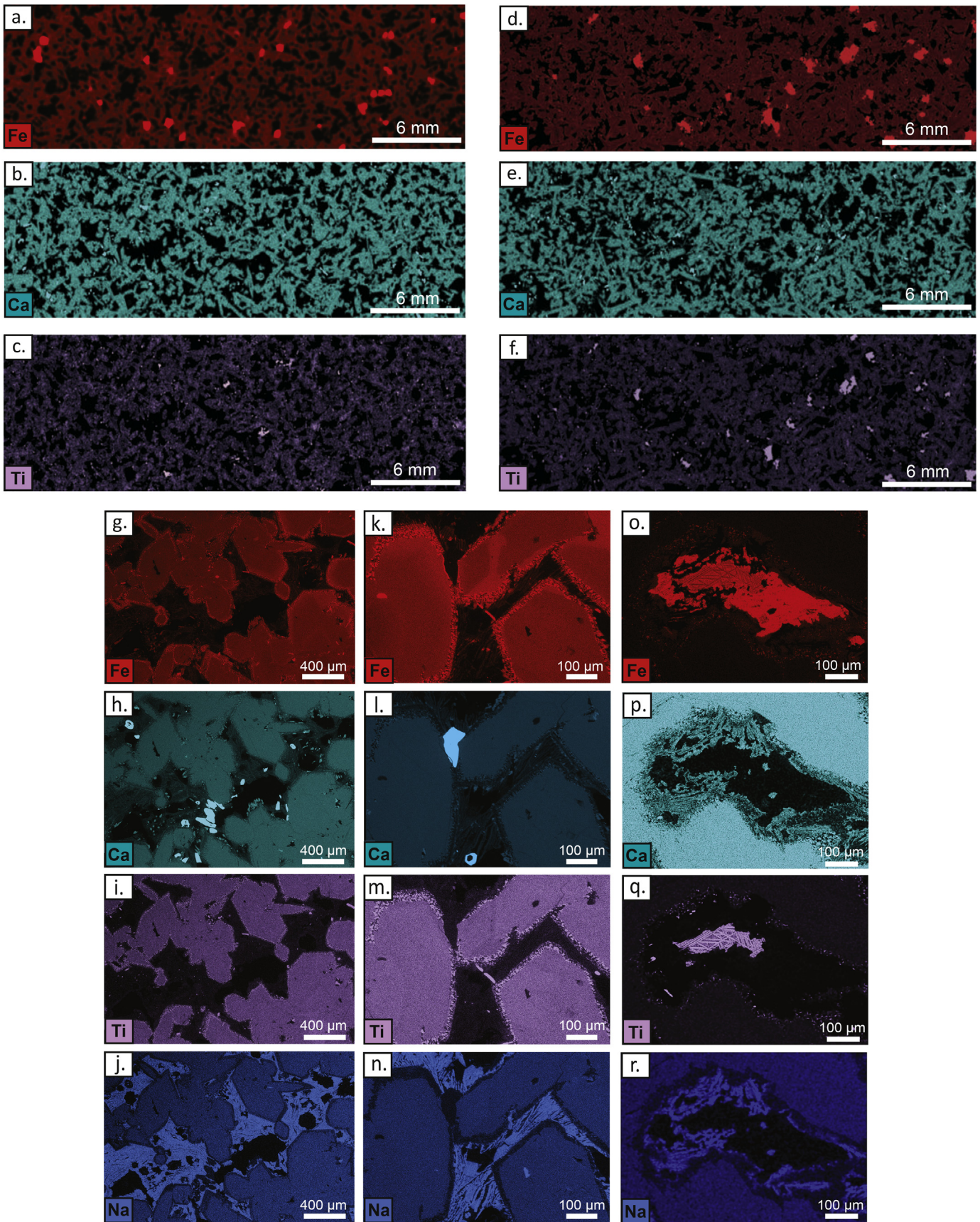


Fig. 4. a-f Whole section μ XRF elemental maps for two hornblende samples. Results from one section are shown on the left, the other on the right. Selected elements shown here are Fe (red), Ca (light blue), and Ti (purple). Regions of higher elemental concentration appear brighter. g-r SEM-EDS was performed to elementally map distinct mineral phases at a smaller scale and at a higher resolution than by μ XRF. g-j SEM-EDS maps of Fe (red), Ca (light blue), Ti (purple) and Na (dark blue) demonstrate subtle compositional variations within the hornblende grains where abundances of Fe are higher nearer the rims. k-n Euhedral hornblendes shown at higher magnification where the compositional variations in Fe within the grain, and higher concentrations of Na in the interstitial regions, are highlighted. o-r Representative SEM-EDS maps for minor titanomagnetite. Rhombohedral ilmenite exsolution lamellae is clearly discernible in the Ti (purple; q) map.

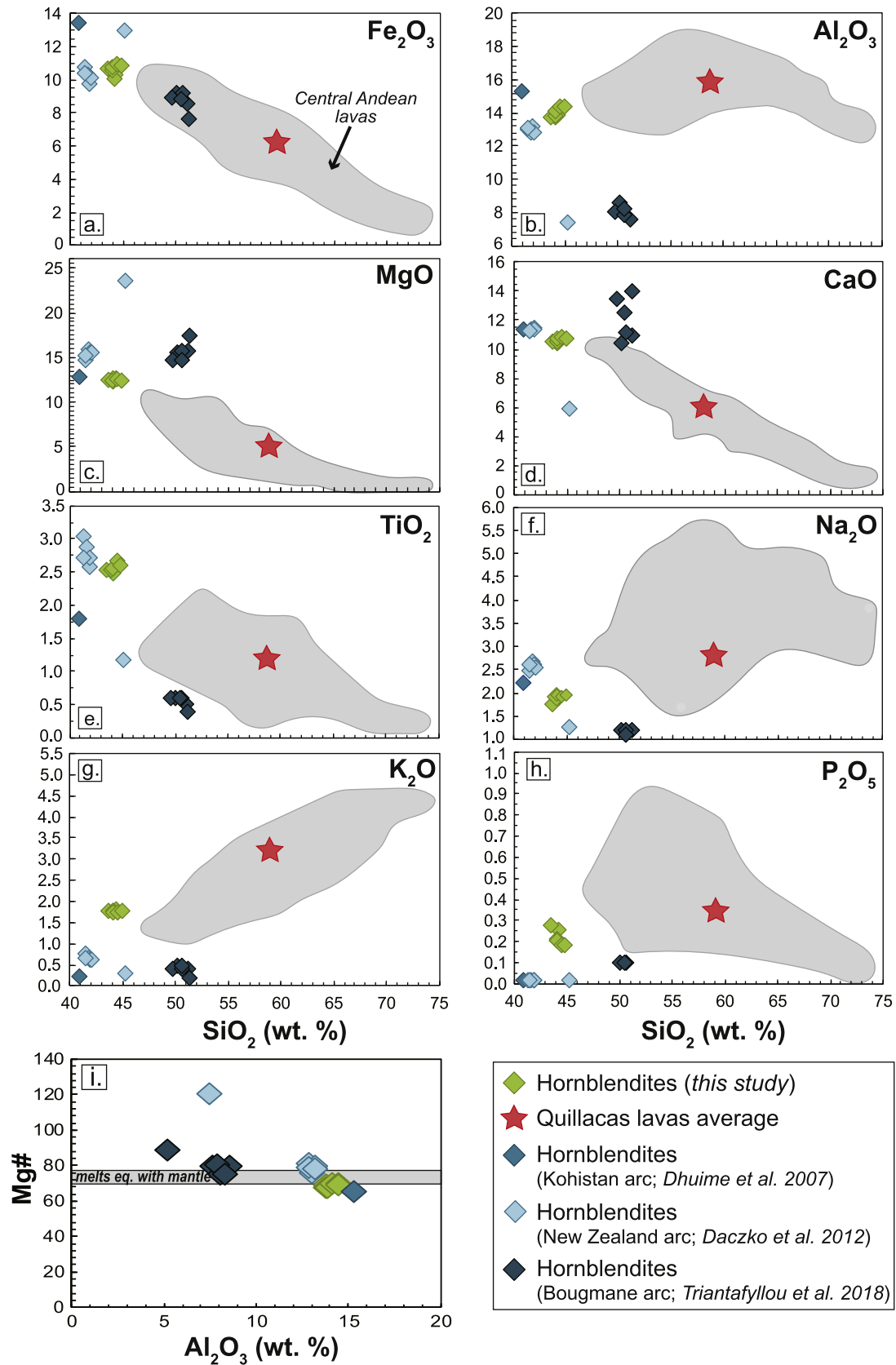


Fig. 5. a-h Major element oxide diagrams. Grey shaded field represents Central Andean lavas (<2 Ma old) where “Central Andean” refers to the region from 13–27°S and 66–74°W. Included in this diagram is the average composition for Quillacas host lavas (red star) as well as hornblendites from other arcs across the world (New Zealand arc, Kohistan arc, and Bougmane arc). **i** Al₂O₃ vs. Mg# illustrating the range (grey field) at which melts equilibrate with mantle (after *Klaver et al., 2017*).

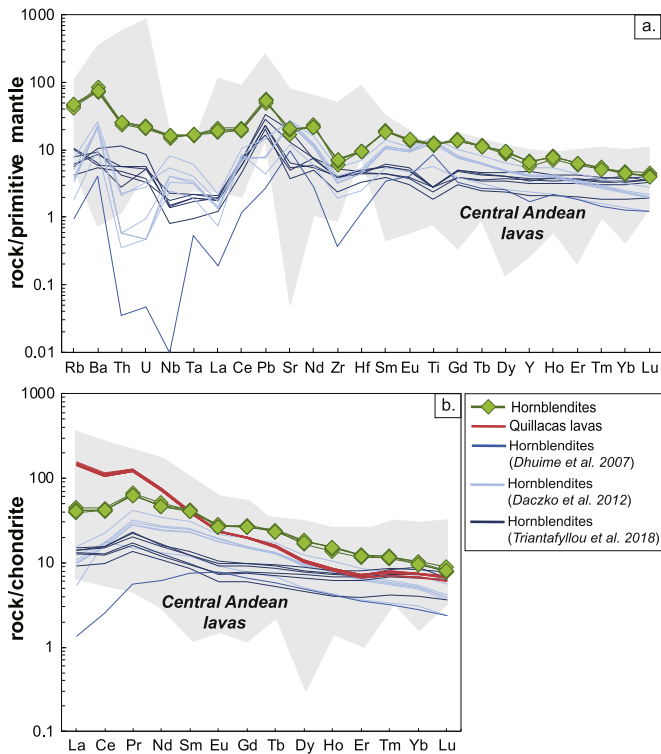


Fig. 6. **a** Primitive mantle normalized multi-element patterns for sampled hornblendites. Grey shaded region represents Central Andean trace element signatures for volcanic rocks <2 Ma old. Included in this diagram are hornblendites from New Zealand arc, Kohistan arc, and Bougmene arc for comparison (see text for discussion). Primitive mantle normalizing values from McDonough (1991). **b** Chondrite-normalized rare-earth element (REE) patterns for sampled hornblendites and Quillacas volcanic host rocks. Also included in this diagram are hornblendites from New Zealand arc, Kohistan arc, and Bougmene arc (see text for discussion). Chondrite normalizing values from Nakamura (1974).

MREE enrichment (Sm_N/Dy_N : 2.08–2.63), and HREE depletion (Dy_N/Lu_N : 1.88–2.72). Negative Eu anomalies (Eu/Eu^*) are consistently observed and range from 0.88–0.97 ($n = 118$, with one value > 1 at 1.02; Fig. 7a–c). This likely implies fractionation of Eu by plagioclase.

Apatites are consistently present as an accessory phase throughout the hornblende samples. Apatite trace element data are presented in Table 3 of the Supplementary Material. Their chondrite normalized REE signatures are summarized in Fig. 7e–g. As expected for apatite, significant LREE enrichment is exhibited with $(La/Sm)_N$ ranging from 3.4 to 6.4. Negative Eu anomalies are consistently observed and range from 0.52–0.89 ($n = 139$). This again likely implies fractionation of Eu by plagioclase. No significant differences in the REE chemistries of the analyzed apatite populations are observed, as is also the case with the sampled amphiboles (Fig. 7d).

Sodic plagioclase is consistently present as an interstitial phase (Figs. 2, 4). Plagioclase trace element data is presented in Table 4 of the Supplementary Material. Sampled grains are characteristically LREE-enriched with $(La/Sm)_N$ ranging from 1.07 to 52.5 (Fig. 7i–k). The most notable features of these patterns however are the consistently prominent positive Eu-anomalies which range from 1.1 to 97.5 ($n = 193$, with one value at 243; Fig. 7i–k). No significant differences in the REE chemistries of the analyzed plagioclase populations are observed (Fig. 7l).

The negative Eu-anomalies in the bulk hornblendites, amphiboles, and apatites are consistent with a magmatic environment in which plagioclase is fractionating. The plagioclase present in the hornblendites crystallized relatively late-stage. This is supported by its interstitial and anhedral nature, in addition to its sodic composition, consistent with fractionation from a differentiated melt (Fig. 4).

4.4. Bulk Sr-Nd-Pb isotopic characteristics

With respect to $^{87}Sr/^{86}Sr$, sampled hornblendites ($n = 7$) are relatively non-radiogenic at 0.707291–0.707314 with corresponding $^{143}Nd/^{144}Nd$ at 0.512271–0.512316 relative to host QL signatures (Fig. 8a). In comparison, host QL lavas ($n = 11$) exhibit $^{87}Sr/^{86}Sr$ values of 0.709128–0.710182 and corresponding $^{143}Nd/^{144}Nd$ at 0.512145–0.51229. A slightly negative relationship with respect to Sr-Nd isotopic systematics is noted between the hornblendites and QL volcanic rocks. For further comparison, Central Andean compositional fields for Nevados de Payachata, Ollagüe, CVZ ignimbrites, Charcani gneiss, and Tata Sabaya are shown in Fig. 8a (after Davidson and de Silva, 1995). The Sr-Nd isotopic compositions of Andean mantle xenoliths are also shown in Fig. 8a and record a broad range of Sr-Nd isotopic signatures from 0.5124–0.5139 and 0.7020–0.7120, respectively (Conceição et al., 2005; Jalowitzki et al., 2017; Lucassen et al., 2005). The majority of these samples exhibit more radiogenic $^{143}Nd/^{144}Nd$ and less radiogenic $^{87}Sr/^{86}Sr$ signatures than sampled hornblendites although two spinel lherzolites (Conceição et al., 2005) and three peridotites (Lucassen et al., 2005) exhibit similar $^{87}Sr/^{86}Sr$ signatures (0.7065–0.7075). These sample suites are associated with the late Cretaceous rift system of NW Argentina, at the edge of the Cenozoic Andean plateau. Compositions of upper and lower crustal reservoirs for this region of the Central Andes (proposed in Davidson and de Silva, 1995) are also shown in Fig. 8a: $^{87}Sr/^{86}Sr > 0.71$ at $^{143}Nd/^{144}Nd < 0.5122$ and $^{87}Sr/^{86}Sr < 0.706$ and $^{143}Nd/^{144}Nd < 0.5122$, respectively. While Nd isotopic signatures do not work to discriminate between crustal reservoirs, the Sr isotopic signatures of the hornblendites are consistent with values recorded by a mid-lower crust reservoir (Davidson and de Silva, 1995).

Lead (Pb) isotopic variation with respect to $^{207}Pb/^{204}Pb$ vs. $^{206}Pb/^{204}Pb$ is summarized for the hornblendites ($n = 4$) in Fig. 8b. Samples vary from 15.58 to 15.77 at 18.52 to 18.54, respectively. The hornblendites' host QL lavas record $^{207}Pb/^{204}Pb$ values of 15.65–15.68 and $^{206}Pb/^{204}Pb$ values of 18.44–18.72. The same suite of data with respect to $^{208}Pb/^{204}Pb$ vs. $^{206}Pb/^{204}Pb$ is shown in Fig. 8c. Hornblendites range from 38.67–38.73 ($^{208}Pb/^{204}Pb$) and 18.52–18.54 ($^{206}Pb/^{204}Pb$), whereas host QL lavas range from 38.95 to 39.00 and 18.44–18.72, respectively. Sampled hornblendites therefore overlap QL lavas with respect to $^{206}Pb/^{204}Pb$ signatures but differ slightly with respect to $^{207}Pb/^{204}Pb$ and $^{208}Pb/^{204}Pb$. In both cases, the hornblendites are comparatively less radiogenic. Central Andean compositional fields for Nevados de Payachata, Ollagüe, CVZ ignimbrites, Charcani gneiss, and Tata Sabaya are shown in Fig. 8b–c (after Davidson and de Silva, 1995) for further comparison. With respect to Pb isotopes, Andean mantle xenoliths show $^{206}Pb/^{204}Pb$ ranges from 16.55 to 25.55, $^{207}Pb/^{204}Pb$ ranges from 15.48 to 15.70, and $^{208}Pb/^{204}Pb$ signatures range from 36.25 to 50.20. It is noted here that four Pb isotopic values from Lucassen et al. (2005) have not been included in Fig. 8b–c due to their highly radiogenic values. As discussed in Lucassen et al. (2005), these highly radiogenic Pb isotopic compositions could be due to the existence of two distinct Pb sources with similar U/Pb but different Th/Pb ratios. The hornblendites' $^{207}Pb/^{204}Pb$ and $^{206}Pb/^{204}Pb$ signatures are most similar to spinel lherzolite xenoliths studied in Jalowitzki et al. (2017) collected 30 km SE from Coyhaique, Chile whereas $^{208}Pb/^{204}Pb$ signatures are slightly higher and overlap those of several CVZ peridotite xenoliths studied by Lucassen et al. (2005).

5. Discussion

5.1. The origin of amphibole in Central Andean hornblendites: chemistries and textures

The nature of the melt from which the amphiboles in the QL hornblendites originated is evaluated in Fig. 9a–b. If amphibole crystallization was associated with fluid metasomatism, low REE contents

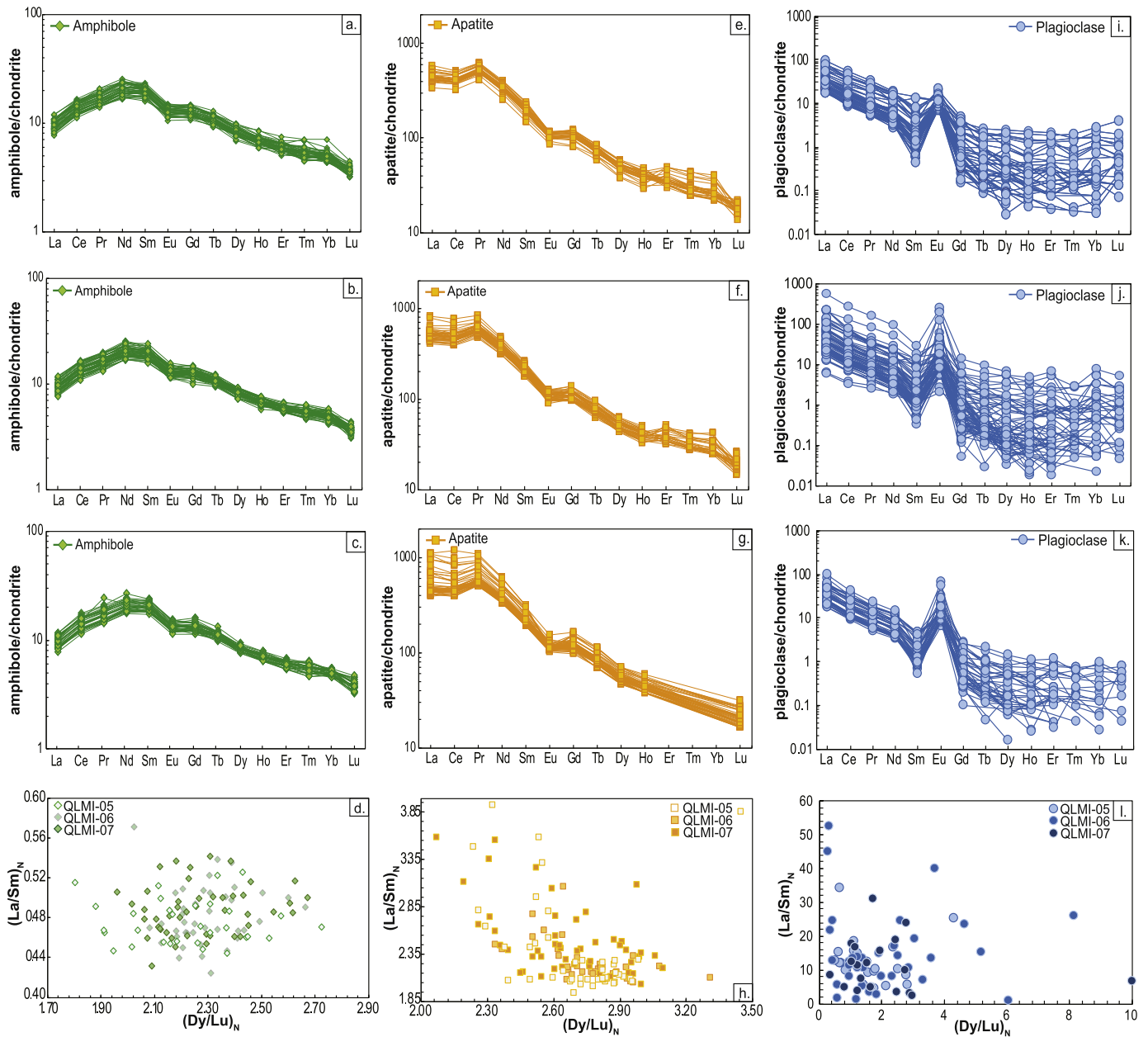


Fig. 7. In-situ trace element data for amphiboles and apatites within three hornblende samples. Rows correspond to data from the same sample. **a–c** Chondrite normalized rare-earth elements (REE) diagram for amphiboles (green). **d** $(La/Sm)_N$ vs. $(Dy/Lu)_N$ diagram including amphibole values for three hornblende samples denoted by the different shades of green. **e–g** Chondrite normalized rare-earth elements (REE) diagram for apatites (orange). **h** $(La/Sm)_N$ vs. $(Dy/Lu)_N$ diagram including apatite values for three hornblende samples denoted by the different shades of orange. **i–k** Chondrite normalized rare-earth elements (REE) diagram for plagioclase feldspars (blue). **l** $(La/Sm)_N$ vs. $(Dy/Lu)_N$ diagram including plagioclase values for three hornblende samples denoted by the different shades of blue. Chondrite normalizing values from Nakamura (1974). (For interpretation of the references to colour in this figure legend, the reader is referred to the web version of this article.)

would be expected due to the low solubility of these elements in aqueous fluids in comparison to silicate melts (Bali et al., 2018). Amphibole crystallization from a silicate melt is therefore demonstrated in Fig. 9a where LREE/HREE enrichment is shown $(La/Yb)_N$. From Powell et al. (2004), $(La/Yb)_N$ values <5 are consistent with amphibole crystallization from a silicate melt, which is observed for all analyzed amphiboles from the hornblendites. Evidence of crystallization from a silicate melt is also supported by considering $(La/Yb)_N$ vs. Ti/Eu (ppm) signatures (Fig. 9a). In addition, if the cumulus amphiboles were associated with precipitation from a fluid, then enrichment in fluid-mobile elements would be expected (e.g. Pb, Rb). In Fig. 9b, $(Pb/Ce)_N$ values are used to evaluate this: amphiboles predominantly have $(Pb/Ce)_N$ values <0.6 .

This is lower than primitive mantle (0.71 from McDonough and Sun, 1995) and consistent with crystallization from a melt as opposed to a $(H_2O$ -rich) fluid (Bali et al., 2018).

Temperature estimates of amphibole crystallization are summarized in Fig. 9c and were calculated based on wt% TiO_2 contents (after Ernst and Liu, 1998). As shown, temperatures range from 700 to 764 °C over a limited range of wt% TiO_2 values (1.1 to 1.5, $n = 118$; Supplementary Table 2). With respect to the Central Andean geothermal gradient, a difference in temperature of 1041 to 141 °C exists between the base and upper part of the crust at 70 km and 5 km (Giese, 1994). Assuming a T gradient of ~ 13.85 °C/km, depth of crystallization for the amphibole population is estimated between 50 and 55 km, which corresponds to

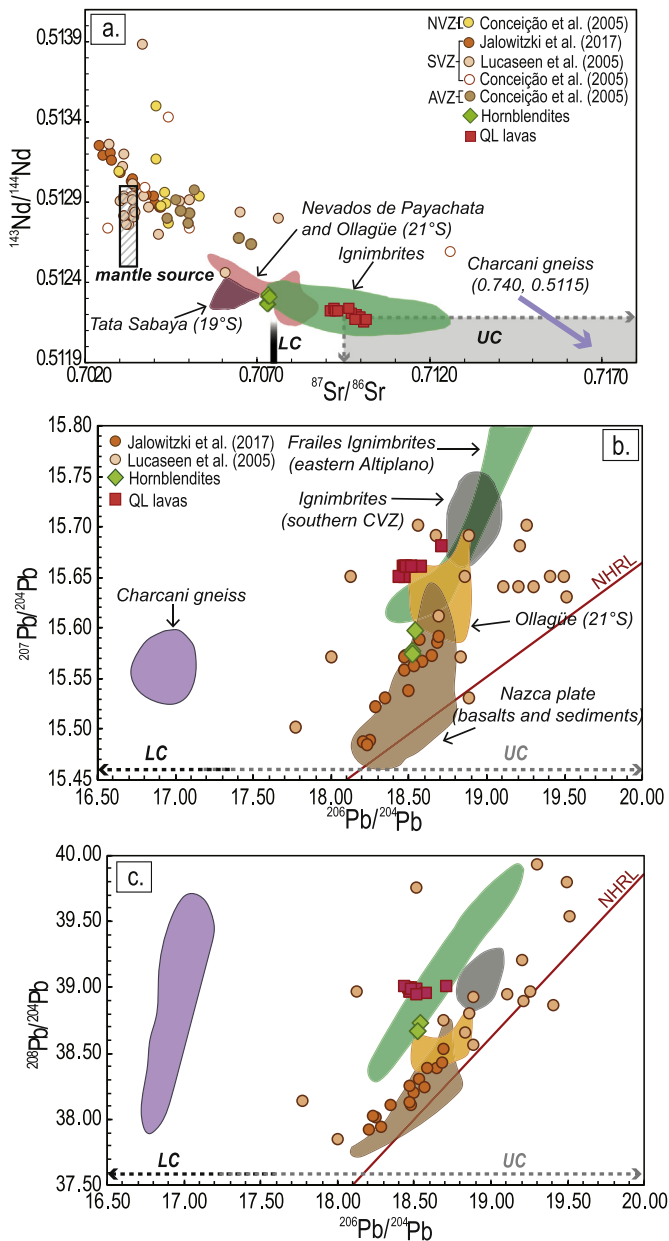


Fig. 8. a $^{87}\text{Sr}/^{86}\text{Sr}$ vs. $^{143}\text{Nd}/^{144}\text{Nd}$ isotopic variation diagram. b $^{207}\text{Pb}/^{204}\text{Pb}$ vs. $^{206}\text{Pb}/^{204}\text{Pb}$ isotopic variation diagram. c $^{208}\text{Pb}/^{204}\text{Pb}$ vs. $^{206}\text{Pb}/^{204}\text{Pb}$ isotopic variation diagram. Data from the hornblende host lavas at Quillacas (pink squares) are included in the three graphs. Regional crustal (LC: lower crust; UC: upper crust) and compositional fields from a variety of localities across Bolivia, Southern Peru, and Chile from Davidsson and de Silva (1995) are included here. Literature data for Andean mantle xenoliths is also included for comparison. Four Pb analyses not shown from Lucassen et al. (2005) due to highly radiogenic values (>20.70 for $^{206}\text{Pb}/^{204}\text{Pb}$, >42.20 for $^{208}\text{Pb}/^{204}\text{Pb}$ and >15.75 for $^{207}\text{Pb}/^{204}\text{Pb}$, see text for discussion). Mantle xenoliths from Conceição et al. (2005) (yellow circles) are found in five localities: Mercaderes, Colombia (NVZ), Agua Poca and Cerro del Mojon, Chile (SVZ), Lote 17 and Cerro Redondo, Argentina (AVZ). Lucassen et al. (2005) mantle xenoliths (light orange circles) are from Las Conchas Valley, Argentina (CVZ). Mantle xenoliths from Jalowitzki et al. (2017) (orange circles) exist in the Chilean back-arc of the SVZ. Lithological compositions for the mantle xenoliths include peridotite xenoliths, carbonatized xenoliths, pyroxenite xenoliths, and spinel-lherzolite xenoliths. The Northern Hemisphere Reference Line (NHRL) is included in b and c (Hart, 1984). (For interpretation of the references to colour in this figure legend, the reader is referred to the web version of this article.)

mid-lower crustal depths in this region. Therefore, the mid-lower arc crust is proposed to be the origin zone for the hornblendites.

Hornblendes exist as a monomineralic cumulus phase occupying $\geq 90\%$ of the sample while intercumulus sodic plagioclase occupies $\sim 8\%$.

Based on these proportions and observed textural relationships, the hornblendites are classified here as mesocumulates. Therefore, it is inferred that amphibole fractionated and accumulated at depth within the crust, likely settling to the base of a storage reservoir. Here, trapped or migrating intercumulus liquid led to the crystallization of anhedral sodic plagioclase with late-stage crystallization of apatite and titanomagnetite based on the intercumulus nature of all three phases.

One of the most notable features of the cumulus hornblendes is their polycrystalline, 20–40 μm wide, dehydration rims (Fig. 10). Previous work has evaluated the textures of breakdown rims associated with amphiboles in arc magmatic systems and has identified two types defined by their reaction products and accompanying textures (Kuno, 1950; Garcia and Jacobson, 1979). These two types are ‘black’ and ‘gabbroic’. From Kuno (1950) and Garcia and Jacobson (1979), black rims can develop as complete, or near-complete, replacements of amphibole. The reacted product is characterized by fine-grained aggregates composed of pyroxene and Fe-oxides, produced as a result of “dehydration and oxidation during extrusion”, which can disseminate along cleavage planes and interior fractures (De Angelis et al., 2015; Garcia and Jacobson, 1979; Rutherford and Hill, 1993). These processes are interpreted as the result of a decrease in oxygen fugacity ($f\text{O}_2$) and an increase in $f\text{O}_2/f\text{H}_2$ (Kuno, 1950). Gabbroic breakdown rims can also form as complete or near-complete replacements of amphibole but in this case, the replacement product is composed of orthopyroxene, clinopyroxene, plagioclase, and Fe-Ti oxide microlites (De Angelis et al., 2015; Garcia and Jacobson, 1979; Rutherford and Hill, 1993). This reaction product and texture is proposed to be the result of a $f\text{O}_2$ decrease resulting in dehydration of “the coexisting melt produced during magma ascent” (Garcia and Jacobson, 1979; Rutherford and Devine, 2003; Rutherford and Hill, 1993).

The polycrystalline assemblage of pyroxene-plagioclase-oxide in the amphibole breakdown rims classifies them as gabbroic (Fig. 10). This implies direct interaction between a melt and the hornblende cumulates. The observed breakdown of the amphibole rims suggests a decrease in the dissolved water content of a co-existing melt, coupled with interaction with the host magma (Rutherford and Hill, 1993). The pervasively coarse-grained, euhedral nature of the amphibole crystals in the hornblendites indicates that they crystallized in a relatively stable magmatic environment at depth (prolonged crystal residence stage). The production of the breakdown rims is therefore inferred as a late-stage processes during melt mobilization and ascent prior to eruption.

Experiments performed by Rutherford and Hill (1993) demonstrated that amphibole reaction rims with widths greater than 20 μm were consistent with a scenario in which magma took more than 10 days to ascend and erupt. A comprehensive study of rim width measurements for the hornblendites in this work has not been undertaken, but observations and measurements of the rims from the detailed SEM imaging resulted in a range of rim widths from 20 to 40 μm in thickness (see Fig. 10a). Based on preliminary rim widths of studied hornblendes, ascent time can be hypothesized to be between 10 and 18 days from a mid-lower crustal storage zone beneath the QL center. However, a more detailed investigation of the rims via SEM imaging and high-resolution chemical analyses is necessary.

5.2. Oxy-exsolution lamellae in (titano)magnetite

(Titano)magnetite is present as a minor phase throughout the sampled suite and characteristically exhibits rhombohedral oxy-exsolution lamellae (shown earlier in Fig. 3e, f). With decreasing temperatures, the Ti component of magnetite is usually exsolved in the form of ilmenite (as opposed to pyrophanite or geikielite) and has been proposed to occur over temperatures of 400 $^{\circ}\text{C}$ to 700 $^{\circ}\text{C}$ (although Ti solubility is also strongly dependent on the partial pressure of oxygen; Ramdohr, 1969). In the case of rhombohedral oxy-exsolution lamellae in (titano)magnetites, a magnetite host exsolves its residual titanium

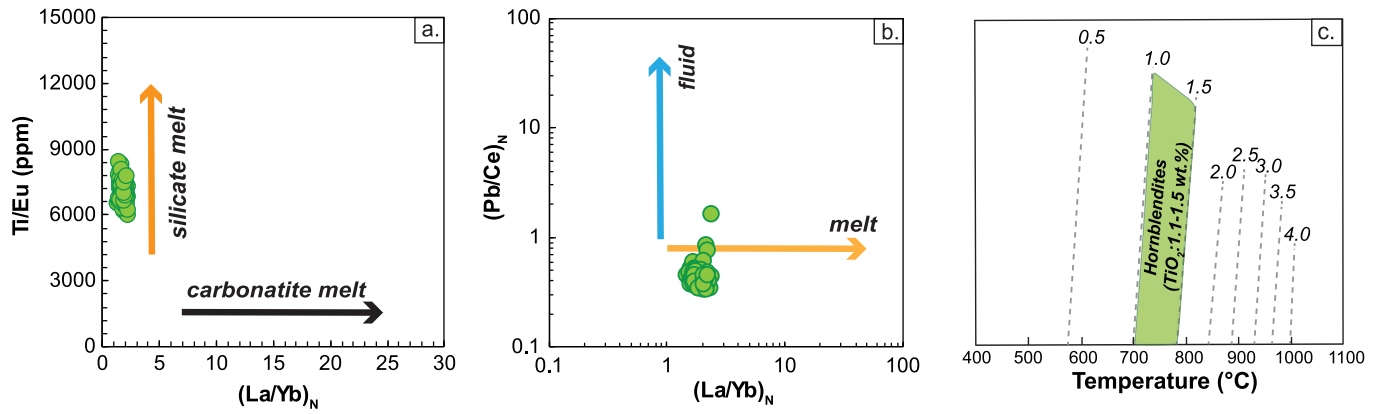


Fig. 9. **a** Amphibole Ti/Eu (ppm) vs. $(La/Yb)_N$ systematics used to discriminate between an origin consistent with a silicate melt (orange arrow) and a carbonatite melt (black arrow). **b** $(Pb/Ce)_N$ vs. $(La/Yb)_N$ for sampled amphiboles used here to discriminate between an origin consistent with a fluid (blue arrow) or melt (orange arrow). Hornblendes from this study are consistent with precipitation from a silicate melt (see text for discussion). Modified from Bali et al. (2018). **c.** Temperature ($^{\circ}C$) of amphibole crystallization based on TiO_2 wt%. The green field represents the wt% TiO_2 of hornblendites from this study (1.1–1.5 wt%, 700–764 $^{\circ}C$; Table 2 of Supplementary Material). Modified from Ernst and Liu (1998). (For interpretation of the references to colour in this figure legend, the reader is referred to the web version of this article.)

towards a Ti-free endmember where the magnetite host accommodates the ilmenite lamellae on the magnetite (111) octahedral planes that are shared with ilmenite (001) planes (Ramdohr, 1969; Robinson et al., 2016). These textures and associated processes have been previously observed and described in other magmatic systems (Ramdohr, 1969; Robinson et al., 2016). In Fig. 11, examples are shown from previously studied gabbros and larvikites (syenites) alongside another example from the Central Andean hornblendites of this study.

The development of rhombohedral oxy-exsolution lamellae in Fe-Ti oxides can be related to local oxidation or reduction conditions during magmatic differentiation (Ramdohr, 1969; Robinson et al., 2016). Associated scenarios have been investigated experimentally by several studies to date (Buddington and Lindsley, 1964; Lattard et al., 2005; Sauerzapf et al., 2008). From these works, it was repeatedly demonstrated that the development of ilmenite oxy-exsolution lamellae could result through oxidation of a cubic titanomagnetite during a temperature decrease. This is exemplified in the ternary phase diagram shown in Fig. 12. Here, three binary solid solutions in $FeO\text{-}\frac{1}{2}Fe_2O_3\text{-}TiO_2$ compositional space are shown with oxidation reactions (oxygen fugacity increasing, at constant Ti/Fe) to the right, and reduction reactions to the left (after Robinson et al., 2016). Highlighted is the scenario in which a titanomagnetite experiences an increase in local oxygen fugacity conditions, promoting an oxidation reaction that results in the exsolution of the Ti component and the generation of ilmenite lamellae. The occurrence of this type of intergrowth, as observed in the (titano) magnetites within the hornblendites, is inferred to represent oxidation during a decrease in temperature in the magmatic system at depth. This is further interpreted to have occurred whilst cooling and crystallization of the hornblendites took place during storage within the arc crust.

5.3. Hornblendites and their significance in the (Central Andean) continental arc crust

The Sr-Nd-Pb isotopic signatures of the hornblendites are broadly consistent with those expected of mid-lower crustal reservoirs in this region (Davidson and de Silva, 1995). It is therefore inferred that the sampled hornblendite cumulates originated within the mid-lower arc crust of the Central Andes. The oxy-exsolution of intercumulus ilmenite from magnetite is consistent with a decrease in temperature (as discussed above) suggesting this intergrowth occurred during late-stage cooling of the cumulate pile. The production of the gabbroic breakdown rims on cumulus amphibole is consistent with dehydration during ascent and are considered to have occurred as the cumulate pile was remobilized during entrainment in the host QL andesites. The

petrogenesis of sampled hornblendites and their inferred route to surface is summarized in Fig. 13.

The generation and stabilization of amphibole-rich cumulates beneath arc systems exerts a fundamental control on the chemistry of arc magmatic products (both intrusive and extrusive) and works to establish a hydrous arc crust at depth (e.g. Daczko et al., 2016; Davidson et al., 2007; Kratzmann et al., 2010; Smith, 2014; Triantafyllou et al., 2018). From Smith (2014), the production of amphibole-rich lithologies at depth within arc systems can result through more than one process, each with its own implications for the role amphibole plays in the sub arc crust. The origin of amphibole can be associated with reaction-replacement processes where clinopyroxene is replaced to varying extents by melt interaction(s) (e.g. Coltorti et al., 2004; Daczko et al., 2012; Daczko et al., 2016; Smith, 2014). Texturally, this process is recorded (or at least can be) through the preservation of relict clinopyroxene and the production of granoblastic textures (see Fig. 2 in Smith, 2014). In this scenario, the “cryptic” role of amphibole in arc systems is associated with mineral-melt reactions in lower crustal mush zones where clinopyroxene is an early fractionating phase and where amphibole is not considered a magmatic phase.

The sampled hornblendites from the QL center in the Central Andes are considered here to be cumulates with amphibole a magmatic phase, which nucleated and crystallized out of a melt at depth. The granular, idiomorphic textures observed, the absence of relict clinopyroxene, and the mesocumulate texture defined by intercumulus plagioclase, apatite, and Fe-Ti oxides all support the interpretation of these hornblendite samples as cumulates. In addition, their magmatic origin is supported by the presence of single twins (see earlier, Supplementary Fig. 2). Beneath this region of the Central Andes, the “amphibole sponge” (Davidson et al., 2007) is proposed to form a cumulate pile at depth. While formation of amphibole via reactive transport (Reiners, 1998) as a melt passes through a clinopyroxene crystal mush cannot be ruled out, the erupted products at QL certainly support the role of hornblendite cumulates at depth as recorded by the “cryptic” amphibole signatures in Central Andean arc magmas. The interpretation that both hornblendite cumulates and clinopyroxene reaction-replacement processes may have an important role in governing magmatic and arc crust differentiation in continental arc settings was recently supported by Xu et al. (2019) where vertical arc sections through the early Mesozoic Gangdese arc were studied. Here, several hornblendite cumulate lithologies were identified (cpx-hornblendite and hornblendite) in addition to non-cumulate lithologies. In cpx-hornblendite lithologies, heteradcumulate textures where cpx crystals (30–40%) were “enclosed” within embayed hornblende were identified whereas in

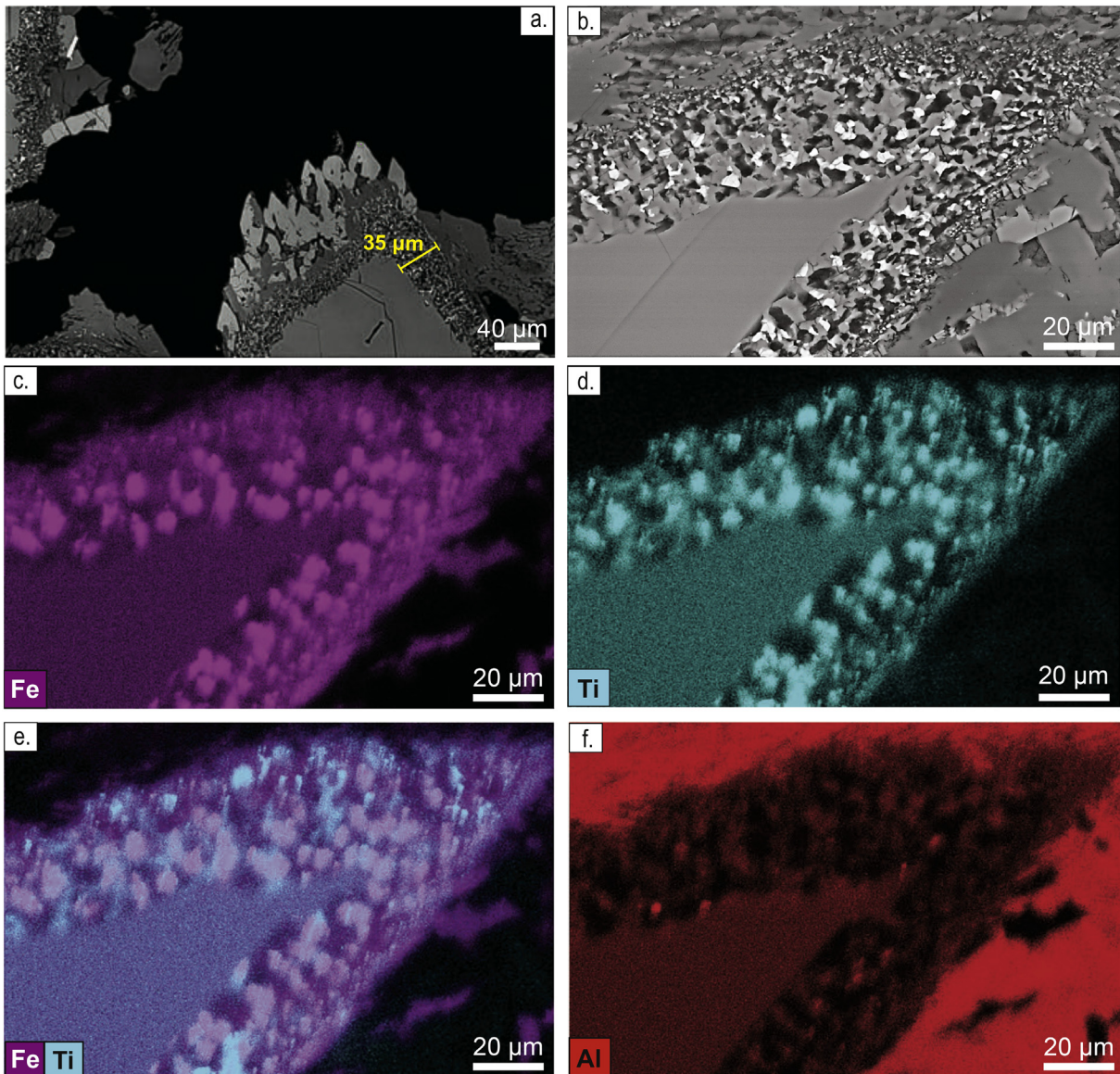


Fig. 10. **a** BSE image of hornblende polymineralic gabbroic dehydration rims. A 35 μm scale bar for the rim is provided in the image. **b** Close-up BSE image of the rims with a scale of 20 μm highlighting the presence of three different phases (pyroxene-plagioclase-oxide) within the rims as interpreted from atomic mass contrast and returned spectra. **c** Corresponding SEM-EDS Fe map of **b**. **d** Corresponding SEM-EDS Ti of **b**. **e** Combined Fe and Ti SEM-EDS map of **b**. **f** Corresponding SEM-EDS Al map of **b**.

hornblendite lithologies, orthocumulate textures with 90% euhedral hornblende were reported. The presence of relict cpx in association with embayed hornblende was inferred to be the result of a reaction between cpx and melt whereas the hornblendite lithologies were interpreted to represent crystallization directly from a melt (Xu et al., 2019). Collectively, this sample suite implies that hornblende as a cumulate phase, and as a reactive-transport product, exists within the volcanic arc crust. While both processes should be considered when evaluating the role of “cryptic” amphibole fractionation during arc magmatism, the hornblendites investigated here support the presence of amphibole-bearing cumulates in this region of the Central Andes.

6. Conclusions

This study presents comprehensive textural and geochemical data for a suite of plagioclase-bearing hornblendite cumulates hosted in andesites erupted from the c. 1.4 Ma Quillacas monogenetic center on the Bolivian Altiplano of the Central Andes. The hornblendites provide

evidence for the ‘cryptic’ fractionation of amphibole from cumulate layers, which are inferred to exist in the mid-lower crust within an open trans-crustal magmatic system in arc environments.

- (1) Sampled hornblendites consist of >90% euhedral hornblende with intercumulus sodic plagioclase along with minor (titano) magnetite and accessory apatite. The trace element compositions and inter element ratios of cumulus amphibole are consistent with their crystallization from a silicate melt, and not a (H_2O -rich) fluid (low $\text{La}_\text{N}/\text{Yb}_\text{N}$ at <5 and $\text{Pb}_\text{N}/\text{Ce}_\text{N}$ lower than primitive mantle). Amphibole TiO_2 contents imply crystallization between 700 and 764 $^\circ\text{C}$ consistent with depths in the arc crust of 50–55 km (based on Central Andean geotherm).
- (2) Sampled hornblendites exhibit bulk Sr-Nd-Pb isotopic signatures that are consistent with their derivation from the mid-lower arc crust based on previous studies of Central Andean magmatic systems.
- (3) Intercumulus (titano)magnetite commonly exhibits oxy-exsolution ilmenite lamellae which has previously been

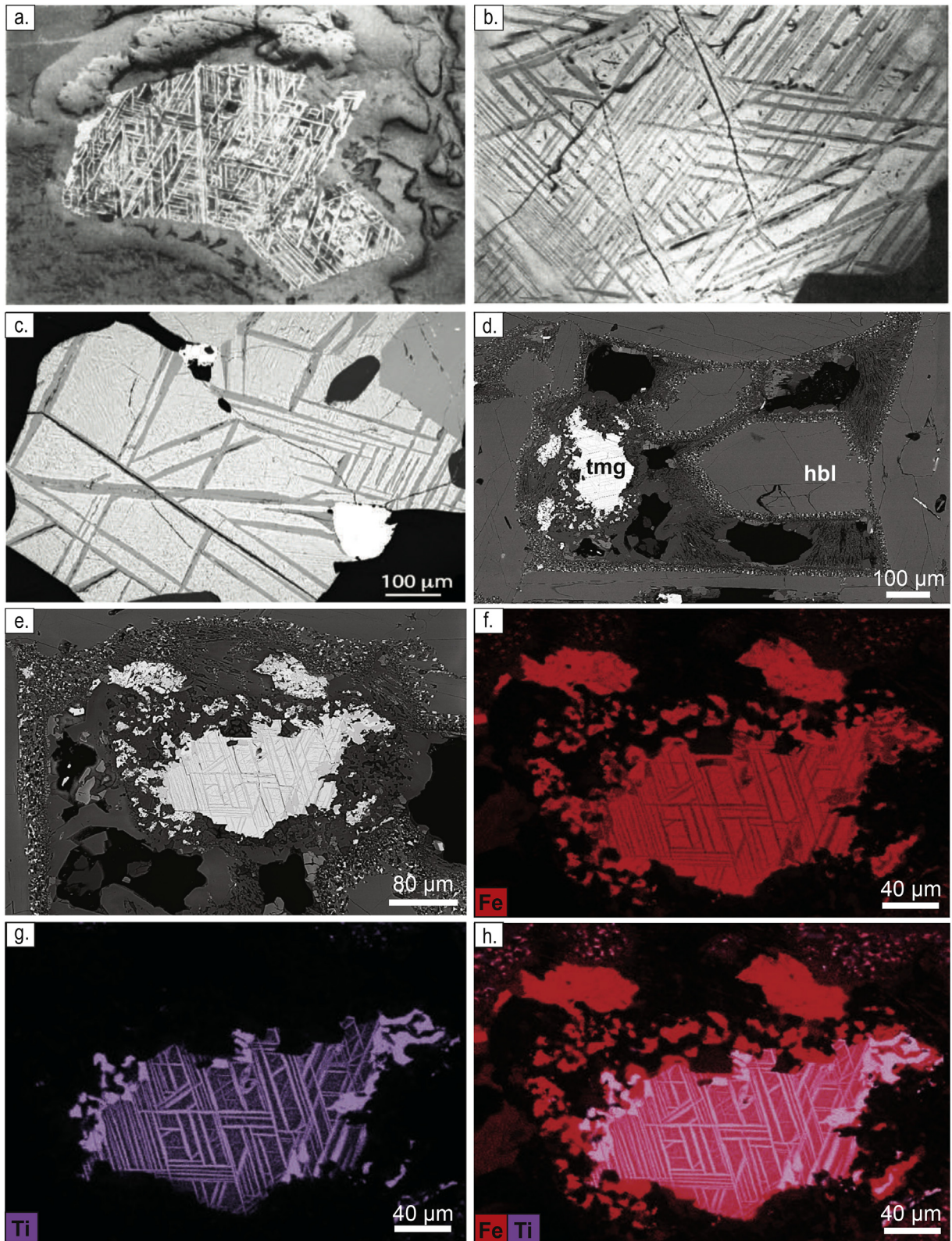


Fig. 11. **a** Example of a gabbro from southwestern Poland exhibiting rhombohedral ilmenite exsolution lamellae (Ramdohr, 1969). **b** Example of a larvikite from southern Norway exhibiting rhombohedral ilmenite exsolution lamellae (Robinson et al., 2016). No scale provided for **a** and **b**. **c** Example of a larvikite from southern Norway exhibiting rhombohedral ilmenite exsolution lamellae (Robinson et al., 2016). **d** BSE image of select region in sample demonstrating hornblendes (hbl) and titanomagnetite (tmg) grains enclosed within a dehydration rim of the hornblende phenocrysts. **e** BSE image of (titano)magnetite grain. **f** Corresponding SEM-EDS Fe map for (titano)magnetite shown in **e**. **g** Corresponding SEM-EDS Ti map for (titano)magnetite shown in **e**. **h** Combined Fe and Ti SEM-EDS map highlighting the habitual rhombohedral ilmenite exsolution lamellae.

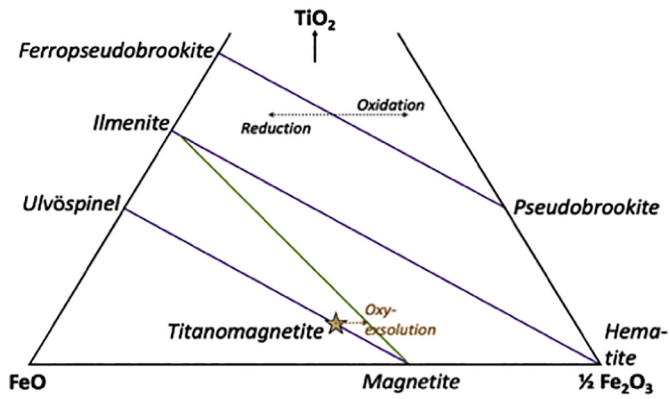


Fig. 12. Ternary diagram defined by FeO, $\frac{1}{2}$ Fe₂O₃, and TiO₂ endmembers. A scenario where oxy-exsolution ilmenite lamellae occurs via oxidation of titanomagnetite is highlighted with a star and arrow. Modified from Robinson et al. (2016).

demonstrated (experimentally) to develop as a result of f_{O_2} increase during magmatic cooling and differentiation. This intergrowth is interpreted as a product of late-stage cooling of the hornblendites during formation of a cumulate pile in the mid-lower arc crust.

- (4) Gabbroic dehydration rims are ubiquitous throughout the amphibole crystal populations. These preserve evidence of remobilization (post-cumulate formation) and dehydration during ascent. The observed reaction products and texture is proposed to be the result of a f_{O_2} decrease during magma ascent, as has been observed in other arc settings (e.g. Mt. St. Helens).
- (5) The idiomorphic, mesocumulate textures of the hornblendites are consistent with the interpretation of these hornblendites as cumulates. No relict clinopyroxene grains are observed indicating that the amphibole formed via direct precipitation from a melt and not via reactive transport processes.

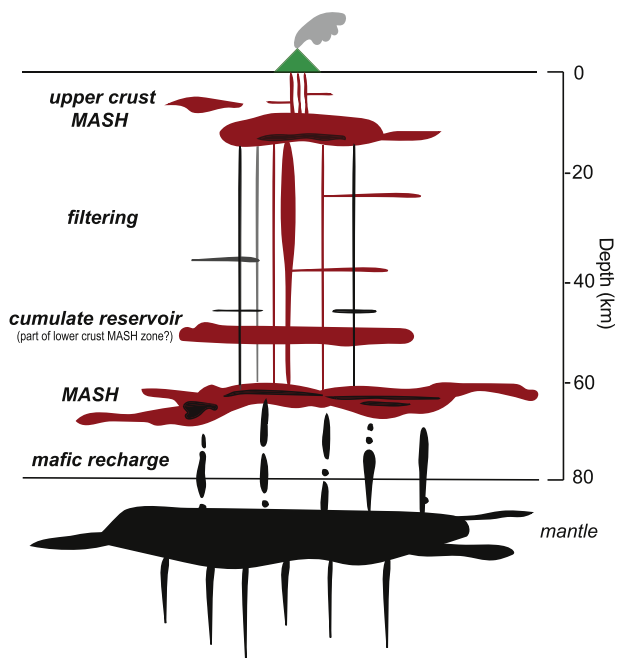


Fig. 13. Schematic diagram of magmatic plumbing system beneath Quillacas volcanic center illustrating different regions of storage throughout the continental arc crust. MASH stands for melting, assimilation, storage, and homogenization processes (after Hildreth and Moorbath, 1988).

Acknowledgements

Dave Kuentz and Masomeh Kousehlar are thanked for their assistance and guidance during sample preparation in the Isotope Geochemistry Laboratory at Miami University and subsequent analyses via TIMS. Mark Krekeler is thanked for his guidance during discussion of images acquired via SEM. Velázquez Santana extends thanks to the Geological Society of America (Student Professional Development Pathways Travel Award program, Mineralogy, Geochemistry, Petrology, & Volcanology Division Travel Grant, and Rocky Mountain Section Travel Grant) and the Graduate School at Miami University. Their financial support permitted attendance and presentation at national meetings during which valuable feedback from the scientific community was solicited prior to submission of this work. We thank two anonymous reviewers for their constructive feedback, comprehensive guidance, and thoughtful commentary that significantly improved the scope of this work.

Appendix A. Supplementary data

Supplementary data to this article can be found online at <https://doi.org/10.1016/j.lithos.2020.105618>.

References

- Adam, J., Green, T.H., Sie, S.H., 1993. Proton microprobe determined partitioning of Rb, Sr, Ba, Y, Zr, Nb and Ta between experimentally produced amphiboles and silicate melts with variable F content. *Chem. Geol.* 109, 29–49. [https://doi.org/10.1016/0009-2541\(93\)90060-V](https://doi.org/10.1016/0009-2541(93)90060-V).
- Bali, E., Hidas, K., Guðfinnsson, G.H., Kovács, Z., Török, K., Román-Alpiste, M.J., 2018. Zircon and apatite-bearing pyroxene hornblendite mantle xenolith from Hungary, Carpathian-Pannonian region. *Lithos* 316, 19–32.
- Barboni, M., Boehnke, P., Schmitt, A.K., Harrison, T.M., Shane, P., Bouvier, A.S., Baumgartner, L., 2016. Warm storage for arc magmas. *Proc. Natl. Acad. Sci.* 49, 13959–13964.
- Beck, S.L., Zandt, G., 2002. The nature of orogenic crust in the Central Andes. *J. Geophys. Res. Solid Earth* 107, 1–16.
- Bishop, B.T., Beck, S.L., Zandt, G., Wagner, L., Long, M., Antonijevic, S.K., Kumar, A., Tavera, H., 2017. Causes and consequences of flat-slab subduction in southern Peru. *Geosphere* 13, 1392–1407.
- Blundy, J., Cashman, K., 2008. Petrologic reconstruction of magmatic system variables and processes. *Rev. Mineral. Geochem.* 69, 179–239.
- Brandmeier, M., Wörner, G., 2016. Compositional variations of ignimbrite magmas in the Central Andes over the past 26 Ma - a multivariate statistical perspective. *Lithos* 262, 713–728.
- Buddington, A.F., Lindsley, D.H., 1964. Iron-titanium oxide mineral and synthetic equivalents. *J. Petrol.* 5, 310–357.
- Cashman, K.V., Sparks, S.J., Blundy, J.D., 2017. Vertically extensive and unstable magmatic systems: a unified view of igneous processes. *Science* 355.
- Coltorti, M., Beccaluva, L., Bonadiman, C., Faccini, B., Ntaflou, T., Siena, F., 2004. Amphibole genesis via metasomatic reaction with clinopyroxene in mantle xenoliths from Victoria Land, Antarctica. *Lithos* 75, 115–139.
- Conceição, R.V., Mallmann, G., Koester, E., Schilling, M., Bertotto, G.W., Rodriguez-Vargas, A., 2005. Andean subduction-related mantle xenoliths: Isotopic evidence of Sr-Nd decoupling during metasomatism. *Lithos* 82, 273–287.
- Cooper, K.M., 2019. Time scales and temperatures of crystal storage in magma reservoirs: implications for magma reservoir dynamics. *Philos. Trans. R. Soc. A Math. Phys. Eng. Sci.* 377.
- Daczko, N., Emami, S., Allibone, A., Turnbull, I., 2012. Petrogenesis and geochemical characterisation of ultramafic cumulate rocks from Hawes Head, Fiordland, New Zealand. *N. Z. J. Geol. Geophys.* 55, 361–374. <https://doi.org/10.1080/00288306.2012.719910>.
- Daczko, N.R., Piazzolo, S., Meek, U., Stuart, C.A., Elliott, V., 2016. Hornblendite delineates zones of mass transfer through the lower crust. *Sci. Rep.* 6, 31369. <https://doi.org/10.1038/srep31369>.
- Davidson, J.P., de Silva, S.L., 1992. Volcanic rocks from the Bolivian Altiplano: Insights into crustal structure, contamination, and magma genesis in the Central Andes. *Geology* 20, 1127–1130.
- Davidson, J.P., de Silva, S.L., 1995. Late Cenozoic magmatism of the Bolivian Altiplano. *Contrib. Mineral. Petrol.* 119, 387–408.
- Davidson, J.P., Hora, J.M., Garrison, J.M., Dungan, M.A., 2005. Crustal forensics in arc magmas. *J. Volcanol. Geotherm. Res.* 140, 157–170.
- Davidson, J.P., Tuner, S., Handley, H., Macpherson, C., Dosseto, A., 2007. Amphibole “sponge” in arc crust? *Geology* 35, 787–790.
- De Angelis, S.H., Larsen, J., Coombs, M., Dunn, A., Hayden, L., 2015. Amphibole reaction rims as a record of pre-eruptive magmatic heating: an experimental approach. *Earth Planet. Sci. Lett.* 426, 235–245.
- Dessimo, M., Müntener, O., Ulmer, P., 2012. A case for hornblende dominated fractionation of arc magmas: the Chelan Complex (Washington Cascades). *Contrib. Mineral. Petrol.* 163, 567–589.

- Dewey, J.F., Lamb, S.H., 1992. Active tectonics of the Andes. *Tectonophysics* 205, 79–95. [https://doi.org/10.1016/0040-1951\(92\)90419-7](https://doi.org/10.1016/0040-1951(92)90419-7).
- Dhuime, B., Bosch, D., Bodinier, J.-L., Garrido, C.J., Bruguier, O., Hussain, S.S., Dawood, H., 2007. Multistage evolution of the Jijal ultramafic–mafic complex (Kohistan, N Pakistan): implications for building the roots of island arcs. *Earth Planet. Sci. Lett.* 261, 179–200. <https://doi.org/10.1016/j.epsl.2007.06.026>.
- Ducea, M.N., Saleeby, J.B., Bergantz, G., 2015. The architecture, chemistry, and evolution of magmatic arcs. *Annu. Rev. Earth Planet. Sci.* 34, 10.1–10.33.
- Edmonds, M., Cashman, K.V., Holness, M., Jackson, M., 2019. Architecture and dynamics of magma reservoirs. *Philos. Trans. R. Soc. A Math. Phys. Eng. Sci.* 377.
- Ernst, W.G., Liu, J., 1998. Experimental Phase–Equilibrium Study of Al- and Ti-Contents of Calcic Amphibole in MORB—A Semiquantitative Thermobarometer 83, 952–969.
- Farner, M.J., Lee, C.T.A., 2017. Effects of crustal thickness on magmatic differentiation in subduction zone volcanism: a global study. *Earth Planet. Sci. Lett.* 470, 96–107.
- Fischer, T.P., Marty, B., 2005. Volatile abundances in the sub-arc mantle: insights from volcanic and hydrothermal gas discharges. *J. Volcanol. Geotherm. Res.* 140, 205–216.
- Ganne, J., Bachmann, O., Feng, X., 2018. Deep into magma plumbing systems: Interrogating the crystal cargo of volcanic deposits. *Geology* 46, 415–418.
- García, M.O., Jacobson, S.S., 1979. Crystal clots, amphibole fractionation and the evolution of calc-alkaline magmas. *Contrib. Mineral. Petrol.* 69, 319–327.
- Giese, P., 1994. Geothermal structure of the central andean crust – implications for heat transport and rheology. In: Reutter, K.-J., Scheuber, E., Wigger, P. (Eds.), *Tectonics of the Southern Central Andes: Structure and Evolution of an Active Continental Margin*. Springer Science & Business Media, pp. 69–76.
- Gill, J., 1981. *Orogenic Andesites and Plate Tectonics*. Springer Verlag.
- Hart, S.R., 1984. A large-scale isotope anomaly in the Southern Hemisphere mantle. *Nature* 309, 753–757.
- Hildreth, W., Moorbath, S., 1988. Crustal contributions to arc magmatism in the Andes of Central Chile. *Contrib. Mineral. Petrol.* 98, 455–499.
- Holness, M.B., Stock, M.J., Geist, D., 2019. Magma chambers versus mush zones: constraining the architecture of sub-volcanic plumbing systems from microstructural analysis of crystalline enclaves. *Philos. Trans. R. Soc.* 377.
- Jackson, M.D., Blundy, J., Sparks, R.S.J., 2018. Chemical differentiation, cold storage and remobilization of magma in the Earth's crust. *Nature* 564, 405–409.
- Jalowitzki, T., Gervasoni, F., Conceição, R.V., Orihashi, Y., Bertotto, G.W., Sumino, H., Schilling, M.E., Nagao, K., Morata, D., Sylvester, P., 2017. Slab-derived components in the subcontinental lithospheric mantle beneath Chilean Patagonia: Geochemistry and Sr–Nd–Pb isotopes of mantle xenoliths and host basalt. *Lithos* 292–293, 179–197.
- Kay, S.M., Mpodozis, C., Gardeweg, M., 2014. Magma sources and tectonic setting of Central Andean andesites (25.5–28°S) related to crustal thickening, forearc subduction erosion and delamination. *Geological Society of London. Special Publications* 385, 303–334.
- Kelemen, P.B., Hanghøj, K., Greene, A.R., 2004. One view of the geochemistry of subduction-related magmatic arcs, with an emphasis on primitive andesite and lower crust. In: Rudnick, R.L. (Ed.), *Treatise on Geochemistry*, 2nd edn, pp. 749–805.
- Klaver, M., Matveev, S., Berndt, J., Lissenberg, C.J., Vroon, P.Z., 2017. A mineral and cumulate perspective to magma differentiation at Nisyros volcano, Aegean arc. *Contrib. Mineral. Petrol.* 172, 95. <https://doi.org/10.1007/s00410-017-1414-5>.
- Kratzmann, D.J., Carey, S., Scasso, R.A., Naranjo, J.A., 2010. Role of cryptic amphibole crystallization in magma differentiation at Hudson volcano, Southern Volcanic Zone, Chile. *Contrib. Mineral. Petrol.* 159, 957–1020 23.61.
- Kuno, H., 1950. Petrology of hakone volcano and the adjacent areas, Japan. *GSA. Bulletin* 61, 957–1020. [https://doi.org/10.1130/0016-7606\(1950\)61\[957:POHVAT\]2.0.CO;2](https://doi.org/10.1130/0016-7606(1950)61[957:POHVAT]2.0.CO;2).
- LaTourrette, T., Hervig, R.L., Holloway, J.R., 1995. Trace element partitioning between amphibole, phlogopite, and basanite melt. *Earth Planet. Sci. Lett.* 135, 13–30. [https://doi.org/10.1016/0012-821X\(95\)00146-4](https://doi.org/10.1016/0012-821X(95)00146-4).
- Lattard, D., Sauerzapf, U., Kasemann, M., 2005. New calibration data for the Fe–Ti oxide thermo-oxybarometers from experiments in the Fe–Ti–O system at 1bar, 1000–1308°C and a large range of oxygen fugacities. *Contrib. Mineral. Petrol.* 149, 735–754.
- Lucassen, F., Franz, G., Viramonte, J., Romer, R.L., Dulski, P., Lang, A., 2005. The late cretaceous lithospheric mantle beneath the Central Andes: evidence from phase equilibria and composition of mantle xenoliths. *Lithos* 82, 379–406.
- Marsh, B.D., 2006. Dynamics of magmatic systems. *Geology* 2, 287–292.
- McDonough, W.F., 1991. Chemical and isotopic systematics of continental lithospheric mantle. In: HOA, Meyer, Leonardos, O.H. (Eds.), *Kimberlites, Related Rocks and Mantle Xenoliths*. 1, pp. 478–485 Companhia de Pesquisa de Recursos Minerais, Rio de Janeiro.
- McDonough, W.F., Sun, S.-S., 1995. Composition of the Earth. *Chem. Geol.* 120, 223–253.
- McLeod, C.L., Davidson, J.P., Nowell, G.M., de Silva, S.L., 2012. Disequilibrium melting during crustal anatexis and implications for modeling open magmatic systems. *Geology* 40, 435–438.
- McLeod, C.L., Davidson, J.P., Nowell, G.M., de Silva, S.L., Schmitt, A.K., 2013. Characterizing the continental basement of the Central Andes: Constraints from Bolivian crustal xenoliths. *GSA Bull.* 125, 985–997.
- Nakamura, N., 1974. Determination of REE, Ba, Fe, Mg, Na and K in carbonaceous and ordinary chondrites. *Geochim. Cosmochim. Acta* 38, 757–775.
- Pepper, M., Gehrels, G., Pullen, A., Ibanez-Mejia, M., Ward, K.M., Kapp, P., 2016. Magmatic history and crustal genesis of western South America: Constraints from U–Pb ages and Hf isotopes of detrital zircons in modern rivers. *Geosphere* 12, 1532–1555.
- Plail, M., Edmonds, M., Woods, A.W., Barclay, J., Humphreys, M.C.S., Herd, R.A., Christopher, T., 2018. Mafic enclaves record syn-eruptive basalt intrusion and mixing. *Earth Planet. Sci. Lett.* 484, 30–40.
- Powell, W., Zhang, M., O'Reilly, S.Y., Tiepolo, M., 2004. Mantle amphibole trace-element and isotopic signatures trace multiple metasomatic episodes in lithospheric mantle, western Victoria, Australia. *Lithos*, Trace element fingerprinting: laboratory studies and petrogenetic processes 75, 141–171. <https://doi.org/10.1016/j.lithos.2003.12.017>.
- Ramdohr, P., 1969. *The Ore Minerals and their Intergrowths*. Pergamon Press, Oxford.
- Reiners, P.W., 1998. Reactive melt transport in the mantle and geochemical signatures of mantle-derived magmas. *J. Petrol.* 39, 1039–1061.
- Reubi, O., Blundy, J., 2009. A dearth of intermediate melts at subduction zone volcanoes and the petrogenesis of arc andesites. *Nature* 461, 1269–1273. <https://doi.org/10.1038/nature08510>.
- Rivera, M., Thouret, J.C., Samaniego, P., Le Pennec, J.L., 2014. The 2006–2009 activity of the Ubinas volcano (Peru): Petrology of the 2006 eruptive products and insights into genesis of andesite magmas, magma recharge and plumbing system. *J. Volcanol. Geotherm. Res.* 270, 122–141.
- Robinson, P., McEnroe, S.A., Miyajima, N., Fabian, K., Church, N., 2016. Remnant magnetization, magnetic coupling, and interface ionic configurations of intergrown rhombohedral and cubic Fe–Ti oxides: a short survey. *Am. Mineral.* 101, 518–530.
- Roeder, R., Emslie, R., 1970. Olivine–liquid equilibrium. *Contrib. Mineral. Petrol.* 29, 275–289.
- Rutherford, M.J., Devine, J.D., 2003. Magmatic Conditions and Magma Ascent as Indicated by Hornblende phase Equilibria and Reactions in the 1995–2002 Soufrière Hills Magma. *J. Petrol.* 44, 1433–1453. <https://doi.org/10.1093/ptrology/44.8.1433>.
- Rutherford, M.J., Hill, P.M., 1993. Magma ascent rates from amphibole breakdown: an experimental study applied to the 1980–1986 Mount St. Helens eruptions. *J. Geophys. Res. Solid Earth* 98, 19667–19685.
- Sauerzapf, U., Lattard, D., Burchard, M., Engelmann, R., 2008. The titanomagnetite–ilmenite equilibrium: New experimental data and thermo-oxybarometric application to the crystallization of basic to intermediate rocks. *J. Petrol.* 49, 1161–1185.
- Schleicher, J.M., Bergantz, G.W., Breidenthal, R.E., Burgisser, A., 2016. Time scales of crystal mixing in magma mushes. *Geophys. Res. Lett.* 43, 1543–1550.
- Scruggs, M.A., Putirka, K.D., 2018. Eruption triggering by partial crystallization of mafic enclaves at Chaos Crags, Lassen Volcanic Center, California. *Am. Mineral.* 103, 1575–1590.
- Shane, P., Smith, V.C., 2013. Using amphibole crystals to reconstruct magma storage temperatures and pressures for the post-caldera collapse volcanism at Okataina volcano. *Lithos* 156–159, 159–170.
- Shirey, S.B., Hanson, G.N., 1984. Mantle-derived Archaean monozodiorites and trachyandesites. *Nature* 310, 222–224.
- Sisson, T.W., 1994. Hornblende–melt trace-element partitioning measured by ion microprobe. *Chem. Geol. Trace-element Partitioning with Application to Magmatic Processes* 117, 331–344. [https://doi.org/10.1016/0009-2541\(94\)90135-X](https://doi.org/10.1016/0009-2541(94)90135-X).
- Smith, D.J., 2014. Clinopyroxene precursors to amphibole sponge in arc crust. *Nat. Commun.* 5, 4329.
- Sørensen, E.V., Holm, P.M., 2008. Petrological inferences on the evolution of magmas erupted in the Andagua Valley, Peru (Central Volcanic Zone). *J. Volcanol. Geotherm. Res.* 177, 378–396.
- Szymanowski, D., Wotzlaw, J.F., Ellis, B.S., Bachmann, O., Guillong, M., von Quadt, A., 2017. Protracted near-solidus storage and pre-eruptive rejuvenation of large magma reservoirs. *Nat. Geosci.* 10, 777–782.
- Taylor, S.R., White, A.J.R., 1965. *Geochemistry of andesites and the growth of continents*. Nature 208, 271–273.
- Triantafyllou, A., Berger, J., Baele, J.-M., Diot, H., Ennih, N., Plissart, G., Monnier, C., Watlet, A., Bruguier, O., Spagna, P., Vanduycke, S., 2016. The Tachakoucht–Irirí–Tourtit arc complex (Moroccan Anti-Atlas): Neoproterozoic records of polyphased subduction-accretion dynamics during the Pan-African orogeny. *J. Geodyn. Subduction Orogeny* 96, 81–103. <https://doi.org/10.1016/j.jog.2015.07.004>.
- Triantafyllou, A., Berger, J., Baele, J.-M., Bruguier, O., Diot, H., Ennih, N., Monnier, C., Plissart, G., Vanduycke, S., Watlet, A., 2018. Intra-oceanic arc growth driven by magmatic and tectonic processes recorded in the Neoproterozoic Bougmane arc complex (Anti-Atlas, Morocco). *Precambrian Res.* 304, 39–63. <https://doi.org/10.1016/j.precamres.2017.10.022>.
- Triantafyllou, A., Berger, J., Baele, J.-M., Mattioli, N., Ducea, M.N., Sterckx, S., Samson, S., Hodel, F., Ennih, N., 2020. Episodic magmatism during the growth of a Neoproterozoic oceanic arc (Anti-Atlas, Morocco). *Precambrian Res.* 339, 105610. <https://doi.org/10.1016/j.precamres.2020.105610>.
- Wallace, P.J., 2005. Volatiles in subduction zone magmas: concentrations and fluxes based on melt inclusion and volcanic gas data. *J. Volcanol. Geotherm. Res.* 140, 217–240.
- Weber, M.B.I., Tarney, J., Kempton, P.D., Kent, R.W., 2002. Crustal make-up of the northern Andes: evidence based on deep crustal xenolith suites, Mercaderes, SW Colombia. *Tectonophysics* 345, 49–82.
- Xu, W., Zhu, D.-C., Wang, Q., Weinberg, R.F., Wang, R., Li, S.-M., Zhang, L.-L., Zhao, Z.-D., 2019. Constructing the early Mesozoic Gangdese Crust in Southern Tibet by Hornblende-dominated Magmatic Differentiation. *J. Petrol.* 69, 515–552.
- Zandt, G., Velasco, A.A., Beck, S.L., 1994. Composition and thickness of the southern Altiplano crust, Bolivia. *Geology* 22, 1003–1006.